Graphical Abstract

Adaptive-Fidelity Hydrodynamic Load Calculation for Floating Offshore Wind Turbines: A Physics-Based Switching Framework

Highlights

Adaptive-Fidelity Hydrodynamic Load Calculation for Floating Offshore Wind Turbines: A Physics-Based Switching Framework

[illegible]

- Per-member, per-timestep switching from KC, steepness, and motion
- A KC–steepness fidelity map for regime-dependent Morison model error
- Adaptive correction reduces regular-wave surge but amplifies irregular-wave surge
- Unconditional correction can trigger catastrophic surge resonance

Adaptive-Fidelity Hydrodynamic Load Calculation for Floating Offshore Wind Turbines: A Physics-Based Switching Framework

Jiamin Zhang[1]*, Hudson Reed[2]

[1]Department of Engineering Science, University of Oxford, Parks Road, Oxford, OX1 3PJ, United Kingdom

[2]Department of Engineering Science, University of Oxford, Osney Mead Building, Oxford, OX2 0ES, United Kingdom

---

Abstract

High-fidelity hydrodynamic models for floating offshore wind turbines typically use fixed Morison coefficients, but the appropriateness of these coefficients varies with the flow regime experienced by each structural member. This paper presents a diagnostic and correction framework based on physics-based fidelity indicators: the Keulegan–Carpenter number, wave steepness, and relative motion amplitude—evaluated per member at each time step. A KC–frequency fidelity map, constructed by comparing engineering-model forces (fixed $C_D = 1.0$, $C_M = 2.0$, linear kinematics) against a reference model with experimentally calibrated coefficients from the oscillatory flow experiments of Sarpkaya (1976), quantifies the regime-dependent error of the engineering model across the parameter space. Applied to the OC4 DeepCwind semi-submersible benchmark at 1:50 model scale, the framework identifies that the three offset columns ($D = 12$ m) operate predominantly in the inertia-dominated regime ($KC < 5$), where the engineering model is adequate, while the smaller cross-brace members ($D = 1.6$ m) enter the drag–inertia transition ($KC \approx 10$–20) during severe sea states, where Morison coefficient errors exceed 15%. The per-member switching indicator correctly activates corrections only where needed, with switching functions ranging

*Corresponding author
Email address: j.zhang@eng.ox.ac.uk (Jiamin Zhang)

from 9% in moderate seas to 39% in severe regular waves; for irregular seas, ensemble averaging over 10 random seeds yields switching fractions of 11 ± 1% (operational) to 40.5 ± 0.7% (severe). In regular waves, the adaptive correction reduces the surge RMS by 12% compared to unit/fidelity, as the Sarpkaya coefficients increase drag on the tower/brace members. In irregular seas, however, the corrections amplify the surge response by 90% (operational) to 270% (severe, $p < 0.001$) through difference-frequency excitation of the lightly damped surge natural mode ($f_n = 0.008$). A frozen-switching diagnostic confirms that this amplification is entirely feed-forward, with negligible feedback from state-dependent switching. The full-correction mode, which applies Sarpkaya coefficients unconditionally to all members including the offset columns, exhibits catastrophic resonant instability (10× surge amplification) due to halved drag damping at low KC, demonstrating that targeted, regime-specific correction is essential. While the framework was designed primarily as a diagnostic tool, the results reveal that even targeted corrections produce significant response changes through nonlinear energy transfer, with implications for FOWT design practice.

Keywords: Floating offshore wind turbine; hydrodynamic loads; adaptive fidelity; Keulegan–Carpenter number; coupled simulation; Morison equation

---

1. Introduction

Floating offshore wind turbines (FOWTs) require accurate prediction of hydrodynamic loads for structural design, mooring system sizing, and fatigue life estimation. The industry-standard approach uses mid-fidelity tools based on potential-flow theory augmented with Morison drag, solving the Cummins equation in the time domain (Cummins, 1962; Robertson et al., 2017). While computationally efficient—enabling the hundreds of load cases required by IEC 61400-3-2 (International Electrotechnical Commission, 2019)—these tools rely on constant hydrodynamic coefficients that do not capture the nonlinear variation of forces with flow regime.

terion for determining where and when high-fidelity corrections are required — at the level of individual structural members and time steps — has not been established for FOWT platforms. The present work fills this gap by quantifying the regime-dependent force error through a KC–frequency failure map and using it to drive per-member, per-timestep switching decisions.

This paper proposes a diagnostic and correction framework that evaluates physics-based fidelity indicators — the Keulegan–Carpenter number, wave steepness, and relative motion amplitude — at each structural member and time step. A pre-computed KC–frequency failure map quantifies the regime-dependent error of the standard engineering model (fixed $C_d = 1.0$, $C_m = 2.0$) Morison formulation against a reference model using experimentally calibrated KC-dependent coefficients from the oscillatory flow experiments of Sarpkaya (1976) and Stokes 2nd-order kinematics. When the fidelity indicators exceed critical thresholds, an additive force correction is applied through a smooth blending function.

The primary contribution is the systematic identification of which members, at which time steps, require improved force modelling—a prerequisite for targeted high-fidelity intervention that has not been quantified for semi-submersible platforms.

The paper is organised as follows. Section 2 presents the theoretical background on hydrodynamic load models and develops the switching framework. Section 3 describes the computational methods including the multi-fidelity solver and the failure map construction. Section 4 defines the validation cases based on the OC4 DeepCwind semi-submersible platform. Section 5 presents results for free decay, regular wave, and irregular wave conditions. Section 6 summarises the findings and discusses limitations.

2. Theoretical background

2.1. Hydrodynamic load models for floating offshore wind turbines

The hydrodynamic forces acting on a floating offshore wind turbine (FOWT) platform can be computed at multiple levels of fidelity, each representing a different balance between physical completeness and computational cost. Three principal approaches span the fidelity spectrum: the Morison equation, potential flow theory, and computational fluid dynamics (CFD).

2.1.1. Morison equation

For slender cylindrical members where the diameter D is small relative to the wavelength λ (typically $D/\lambda < 0.2$), the inline hydrodynamic force per unit length is given by the Morison equation (Morison et al., 1950):

$$f(z,t) = \underbrace{\rho C_M \frac{\pi D^2}{4} \dot{u}}_{\text{inertia}} + \underbrace{\frac{1}{2} \rho C_D D |u - \dot{x}| (u - \dot{x})}_{\text{drag}} \tag{1}$$

where ρ is the fluid density, C_M and C_D are the inertia and drag coefficients, u is the undisturbed wave-induced velocity, $\dot{u}$ is its time derivative, and $\dot{x}$ is the structural velocity. The force coefficients depend on the flow regime, characterized principally by the Keulegan–Carpenter number:

$$KC = \frac{u_m T}{D} \tag{2}$$

where u_m is the maximum orbital velocity and T is the wave period. For $KC < 5$, inertia dominates and C_D has minimal influence; for $KC > 20$, drag dominates. In the transition regime $5 < KC < 20$, both components contribute significantly and the coefficients become strongly KC-dependent (Sarpkaya, 1986; Sumer and Fredsøe, 2006).

The Morison equation is computationally inexpensive and well-suited for slender-member forces in operational sea states. However, it neglects diffraction effects on large-diameter members, assumes small relative motion, and uses constant (or at best onset-averaged) coefficients that cannot capture the nonlinear variation of forces with wave steepness or platform motion amplitude.

2.1.2. Potential flow theory

For large-volume structures where diffraction effects are important ($D/\lambda > 0.2$), the hydrodynamic problem is typically solved using linear potential flow theory in the frequency domain. The equation of motion for the floating body in the time domain follows the Cummins equation (Cummins, 1962):

$$(M + A_\infty)\ddot{\xi}(t) + \int_0^t K(t-\tau)\dot{\xi}(\tau)\,d\tau + C\xi(t) = F_{exc}(t) + F_{visc}(t) + F_{moor}(t) \quad (3)$$

where M is the body mass matrix, A_∞ is the infinite-frequency added mass, $K(t)$ is the radiation impulse response (retardation) function computed from frequency-dependent radiation damping $B(\omega)$:

$$K(t) = \frac{2}{\pi}\int_0^\infty B(\omega)\cos(\omega t)\,d\omega \quad (4)$$

C is the hydrostatic restoring matrix, F_{exc} is the wave excitation force (Froude-Krylov plus diffraction), F_{visc} is the viscous drag correction (typically from Morison-type quadratic drag), and F_{moor} is the mooring restoring force.

Linear potential flow captures radiation and diffraction accurately for small-amplitude motions. Second-order extensions via quadratic transfer functions (QTFs) can capture mean drift and slow-drift forces (Pinkster, 1980). However, the theory is fundamentally limited by the assumptions of irrotational flow, the use of weakly nonlinear free-surface conditions, and small body motions relative to the wave amplitude.

2.1.3. Computational fluid dynamics

The full Navier-Stokes equations, solved using the volume-of-fluid (VOF) method for free-surface tracking, provide the most complete description of the wave–structure interaction:

$$\frac{\partial \rho \mathbf{u}}{\partial t} + \nabla\cdot(\rho \mathbf{u} \otimes \mathbf{u}) = -\nabla p + \nabla\cdot\boldsymbol{\tau} + \rho\mathbf{g} \quad (5)$$

$$\nabla\cdot\mathbf{u} = 0 \quad (6)$$

where τ is the viscous stress tensor (augmented by a turbulence model, typically k-ω SST). The free surface is tracked via the VOF equation for the volume fraction α:

$$\frac{\partial\alpha}{\partial t} + \nabla\cdot(\alpha\mathbf{u}) = 0 \quad (7)$$

CFD captures all relevant physics including viscous effects, flow separation, wave breaking, and nonlinear free-surface interaction. Coupled with a rigid-body motion solver, it provides the most accurate prediction of platform response. The computational cost, however, is typically 10^3–10^4 times that of potential-flow-based models, making it impractical for the hundreds of load cases required in FOWT design certification (Robertson et al., 2020).

2.2. Physics-based fidelity indicators

The central premise of this work is that the failure of low-fidelity models is not random but predictable from local flow-regime indicators. We define three dimensionless parameters that govern model applicability.

Keulegan–Carpenter number. As defined in eq. (2), KC characterizes the relative importance of drag versus inertia. For a semi-submersible platform, different structural members experience different local KC values depending on their diameter and the local orbital velocity. The columns (large diameter, $D \approx 12$ m at full scale for the OC5 DeepCwind) operate at low KC (inertia-dominated), while bracing members and heave plates (smaller diameter or sharp edges) can experience $KC > 10$ where Morison coefficient uncertainty is largest.

Wave steepness. The ratio H/λ (wave height to wavelength) quantifies the departure from linear wave theory. For $H/\lambda < 0.02$, linear potential flow provides adequate excitation forces. Above $H/\lambda \approx 0.04$, nonlinear free-surface effects—including wave crest amplification and higher-harmonic forces—become significant and linear superposition underestimates peak loads (Faltinsen, 1990).

Relative motion amplitude. The ratio of platform motion amplitude to a characteristic length (body diameter or wave amplitude) determines whether the small-motion assumption underlying frequency-domain hydrodynamic coefficients is valid. For pitch motions exceeding approximately 5°, the linearized restoring and radiation forces deviate substantially from the nonlinear reality, particularly for semi-submersibles with large waterplane area variations (Robertson et al., 2022).

3.3. Adaptive-fidelity switching framework

We propose a framework that evaluates the fidelity indicators at each time step and for each structural member, and activates high-fidelity corrections only when mid-fidelity models are predicted to be inaccurate. The overall framework is illustrated in Fig. 3. The switching logic operates on a per-member, per-timestep basis, with the platform response feeding back to the fidelity indicators through the instantaneous motion state.

Figure 3: Overview of the adaptive-fidelity hydrodynamic load simulation framework. The wave environment and instantaneous platform motion are used to evaluate physics-based fidelity indicators for each structural member. When the composite indicator Φ_j exceeds unity, localized-based force corrections are applied through a smooth blending function. The failure map (see right) summarizes the regimes where mid-fidelity models are inadequate.

3.3.1. Switching criterion

Define a composite fidelity indicator $\Phi_j(t)$ for the j-th structural member at time t:

$$\Phi_j(t) = \max\left(\frac{KC_j(t)}{KC_{cr}}, \frac{(H/\lambda)(t)}{(H/\lambda)_{cr}}, \frac{\theta_{local}(t)}{\theta_{cr}}\right) \quad (6)$$

where KC_{cr}, $(H/\lambda)_{cr}$, and θ_{cr} are the critical thresholds determined from the failure map (see section 3.2). The local KC for member j is computed from the instantaneous relative velocity between the wave orbital velocity (from the undisturbed wave field evaluated at the member location) and the member velocity:

$$KC_j(t) = \frac{|u_{rel,j}(t)|\,T_p}{D_j} \quad (7)$$

where T_p is the peak spectral period and D_j is the member diameter.

The switching rule for member j at time t is:

$$s_j(t) = \begin{cases} 0 \ \text{(undisturbed)} & \text{if } N_j(t) = 1, \\ 1 \ \text{(interacted)} & \text{if } N_j(t) \geq 2, \end{cases} \tag{10}$$

where $s_j = 0$ retains the engineering model and $s_j = 1$ activates the additive correction.

2.3.2. Additive force correction

When the switching criterion is activated for member j, the total force is computed as

$$\mathbf{F}_j(t) = \mathbf{F}_{eng,j}(t) + \Delta\mathbf{F}_{corr,j}(t) \tag{11}$$

where $\Delta\mathbf{F}_{corr,j}$ is the correction force obtained from a pre-computed lookup table indexed by the local flow parameters $(KC_j, \beta(t), D_j/L)$. This lookup table is constructed from the systematic single-cylinder parametric study described in section 3.2, which compares engineering-model forces against DeepLines reference-model forces.

The correction force is defined as the difference between the reference force and the engineering prediction for the same flow conditions:

$$\Delta\mathbf{F}_{corr}(KC, \beta(t)) = \mathbf{F}_{ref}(KC, \beta(t)) - \mathbf{F}_{eng}(KC, \beta(t)) \tag{12}$$

To avoid discontinuities at the switching boundary, a temporal blending function is applied per member over a transition interval Δt_{blend}:

$$\mathbf{F}_j(t) = \mathbf{F}_{eng,j}(t) + w_j(t)\,\Delta\mathbf{F}_{corr,j}(t) \tag{13}$$

where $w_j(t)$ ramps smoothly between 0 and 1 using a symmetric cosine function. On activation ($N_j \geq 2$):

$$w_j(t) = \frac{1}{2}\left[1 - \cos\left(\pi \frac{t - t_{on}}{\Delta t_{blend}}\right)\right], \quad t_{on} \leq t \leq t_{on} + \Delta t_{blend} \tag{14}$$

and on deactivation ($N_j = 1$):

$$w_j(t) = \frac{1}{2}\left[1 + \cos\left(\pi \frac{t - t_{off}}{\Delta t_{blend}}\right)\right], \quad t_{off} \leq t \leq t_{off} + \Delta t_{blend} \tag{15}$$

Both ramps are C^1 continuous at the boundaries ($w = 0$ and $w = 1$), ensuring smooth force transitions without derivative discontinuities.

3. Computational methods

3.1. Hydrodynamic time-domain solver

The hydrodynamic model solves the Cummins equation (eq. (5)) in the time domain using a fourth-order Runge–Kutta scheme. The convolution integral in the radiation force is approximated using a state-space representation (Perez and Fossen, 2009):

$$\dot{\mathbf{x}}_r = \mathbf{A}_r \mathbf{x}_r + \mathbf{B}_r \dot{\mathbf{x}}, \qquad \mathbf{F}_{rad}(t) = \mathbf{C}_r \mathbf{x}_r \tag{16}$$

where $\mathbf{A}_r$, $\mathbf{B}_r$, $\mathbf{C}_r$ are obtained by fitting the retardation function $K(t)$ using the method of Perez and Fossen (2009). This avoids the computational cost of evaluating the convolution integral at each time step.

Wave excitation forces are computed using a Froude–Krylov approximation with a frequency-independent diffraction correction factor of [illegible] applied to the total submerged volume:

$$F_{exc}(t) = [illegible] \tag{17}$$

where A is the wave amplitude, k the wavenumber, and V_{sub} the total submerged volume. This approximation captures the frequency dependence of the excitation force at leading order but does not account for the frequency-dependent diffraction that a potential-flow solver (e.g., WAMIT or NEMOH) would provide. For irregular waves, the excitation is computed as a spectral sum of $N = 200$ frequency components with per-component wavenumber and depth transfer functions. The implications of this approximation are discussed in section 6.

A temporal convergence study confirmed that the time step $\Delta t = [illegible]$ (model scale) produces converged results: halving the time step to $\Delta t = [illegible]$ changes the RMS surge, heave, and pitch responses by less than [illegible] across all simulation modes and wave conditions, with an observed convergence order consistent with the fourth-order Runge–Kutta scheme.

Viscous drag on the structural members uses the Morison equation with a fixed drag coefficient $C_D = 1.0$ and a relative-velocity formulation:

$$F_{drag} = \frac{1}{2}\rho C_D D |u_{rel}| u_{rel}, \quad u_{rel} = u_{wave} - \dot{x} \tag{10}$$

where u_{wave} is the local wave particle velocity at individual depth and $\dot{x}$ is the body velocity. The fixed $C_D = 1.0$ value matches the engineering baseline used in the failure map (section 3.3), ensuring that the adaptive correction is purely additive: the total corrected drag coefficient equals $C_D + \Delta C_D$ where $\Delta C_D = C_{D,\mathrm{Sarpkaya}}(KC) - 1.0$.

3.3. Failure map construction

The KC-frequency failure map is constructed from a parametric study of hydrodynamic forces on a circular cylinder. Three levels of force modelling are used:

Reference model: Stokes 2nd-order wave kinematics with experimentally calibrated force coefficients from the oscillatory-flow experiments of Sarpkaya (1976, 1986). The Sarpkaya coefficients capture the KC-dependent variation of C_D and C_M measured at Reynolds numbers $Re \sim 10^4$–10^5, including the drag-inertia transition at $5 < KC < 20$. This model includes crest-trough asymmetry from the second-order wave kinematics and serves as the primary reference for the failure map.

Engineering model: Linear (Airy) wave kinematics with fixed coefficients $C_D = 1.0$ and $C_M = 2.0$, representing the default values recommended by DNV GL (2014) and used in standard FOWT design tools.

The normalised force error between the engineering and reference models defines the failure map:

$$\varepsilon(KC, H/\lambda) = \frac{|F_{eng} - F_{ref}|}{|F_{ref}|} \tag{11}$$

The critical thresholds KC_c and $(H/\lambda)_c$ are defined as the parameter values where ε exceeds 15%, a level at which the engineering model can no longer be

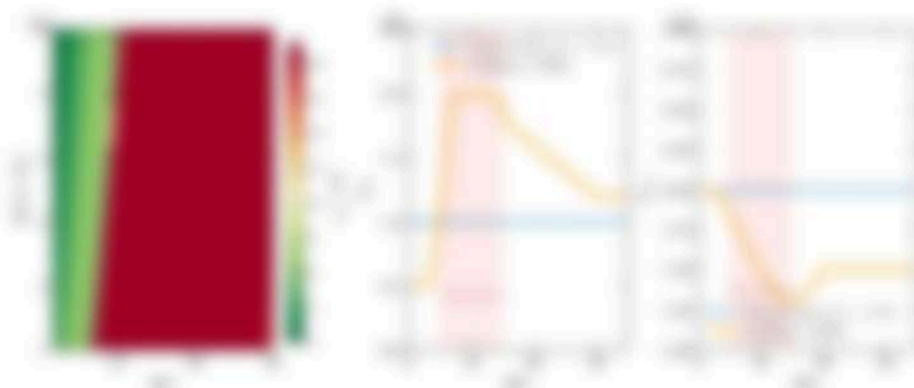

verification campaigns. The platform comprises three offset columns of diameter 12 m (full scale) arranged at 120° intervals around a central column of diameter 6.5 m, connected by pontoons and cross-braces. Heave plates of diameter 24 m are located at the base of the offset columns. The platform is moored by a three-line catenary system.

All simulations are conducted at 1:50 model scale (Froude scaling) to enable direct comparison with the OC5 Phase II experimental data obtained at the MARIN wave basin (Robertson et al., 2020). The principal model-scale parameters are summarised in table 1.

Table 1: Semi-submersible principal parameters at 1:50 model scale.

Parameter	Model scale	Full scale
Draft (m)	0.40	20.00
Offset column diameter (m)	0.24	12.00
Centre column diameter (m)	0.13	6.50
Heave plate diameter (m)	0.48	24.00
Displacement (kg)	111.70	1.396×10^7
Water depth (m)	4.00	200.00
Natural periods (from free decay)		
Surge (s)	15.70	111.00
Heave (s)	2.50	17.60
Pitch (s)	3.70	26.10

4.3 Test cases

The validation comprises three categories of tests with increasing complexity, following the approach of the OC4/OC5 campaigns:

- *Free decay tests.* Initial displacement tests in surge, heave, and pitch (one DOF at a time, no waves) to validate the hydrostatic restoring, radiation damping, and viscous drag characteristics of the numerical model. The natural periods and damping ratios are compared with OC5 experimental values.

Regular wave cases. Two regular wave conditions are simulated. The moderate case ($T =$ [illegible], $H =$ [illegible], $H/L =$ [illegible]; full-scale [illegible]) corresponds to OC5 Phase II LC [illegible]. The severe case ($T =$ [illegible], $H =$ [illegible], $H/L =$ [illegible]; full-scale [illegible]) is designed to push the [illegible] members into the KC transition regime. These cases span the range from moderate to severe conditions, where the adaptive framework should demonstrate different fidelity requirements across the structural members.

Irregular wave cases. Two irregular sea states with JONSWAP spectra ($\gamma =$ [illegible]) are simulated, each for a duration of [illegible]T_p. The operational case uses $H_s =$ [illegible] with $T_p =$ [illegible]; the severe case uses $H_s =$ [illegible] with $T_p =$ [illegible].

4.3. Comparison methods

Three simulation approaches are compared for each test case. First, the [illegible] baseline uses the Cummins equation with [illegible] radiation, Morison drag with fixed $C_D =$ [illegible] and $C_M =$ [illegible], and linear mooring restoring (section [illegible]), with no force corrections applied. Second, the adaptive-fidelity approach augments the [illegible] solver with force corrections from the pre-computed lookup table (section [illegible]) when the switching criterion $\mathcal{R}_i(t) \geq 1$ is activated (section [illegible]); the correction accounts for both the drag and inertia coefficient differences (Sarpkaya vs. fixed), applied per member with cosine blending. Third, the full correction mode applies the Sarpkaya-based force correction to all members at all time steps, providing an upper bound on the correction effect without switching. This mode does not invoke a full CFD solver; it applies the maximum available correction from the pre-computed lookup table unconditionally.

The switching thresholds are set to [illegible], corresponding to the onset of the [illegible] regime identified in the KC [illegible]

scale, corresponding to 15.1 s, 17.9 s, and 30.5 s at full scale. These agree with the 1978 experimental values (16.7 s, 17.5 s, 30.4 s; Robertson et al., 2008) to within 2.6%, 2.3%, and 1.2%, respectively.

The logarithmic decrement analysis yields damping ratios of $\zeta_{surge} = 0.0087$ (5 peaks), $\zeta_{heave} = 0.020$ (3 peaks), and $\zeta_{pitch} = 0.080$ (10 peaks). The very low surge damping ($\zeta_s = 0.009$, quality factor $Q = 58$) is significant: it implies that any force perturbation near the surge natural frequency will be amplified substantially, a property that becomes important in the irregular wave results (section 3.4). Physical model tests of the DeepCwind semi-submersible typically report $\zeta_{surge} = 0.03$–0.05 (Coulling et al., 2013); our numerical value of 0.0087 is approximately 4–6× lower, primarily because the model under-counts damping on the hull and large-diameter column surfaces. These damping values, which arise from the combination of radiation damping and viscous drag on the Morison members only, are not calibrated parameters.

3.3. Regular wave response

Figure 5 presents the platform response to severe regular waves ($H = 10$ m, $T = 12$ s at full scale). Three simulation modes are compared: unreliability (no correction), adaptive (correction applied when $\mathcal{R}_i \geq 1$), and full correction (correction applied to all members at all times). The unreliability model predicts an RMS surge displacement of 0.5 mm full scale (0.09 mm model scale). The adaptive mode yields 10.0 mm full scale with corrections active 20% of the time — predominantly on the cross-brace members whose smaller diameter ($D = 1.6$ m full scale) places them in the drag–inertia transition regime ($KC \approx 8$–15). The 18% reduction in adaptive surge relative to unreliability reflects the increased drag damping from the Sarpkaya coefficients ($C_d = 1.5$ at $KC \approx 15$, versus the engineering value of $C_d = 1.0$) applied to the cross-brace members.

The offset columns ($D = 12$ m full scale) operate at low KC ($KC \approx 2.5$) and the framework correctly identifies that the unreliability model is adequate for these members. The heave response is identical across all fidelity levels (19 mm full scale RMS), as heave excitation is dominated by the Froude–Krylov pressure

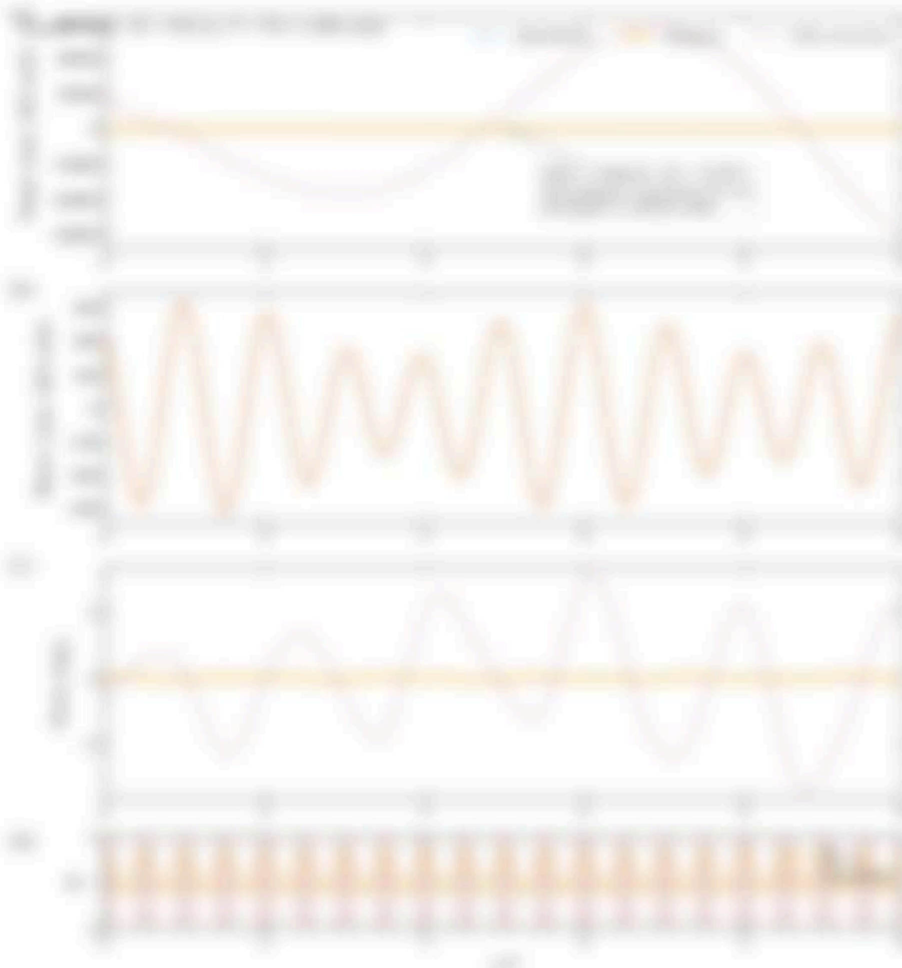

forces, reducing the response. In irregular waves, the intermittent corrections generate broadband difference-frequency forces that excite the lightly damped surge natural mode.

The 10× amplification in full-correction mode reflects the same damping reduction mechanism identified in the regular wave case. The Steadiness correction applied unconditionally to the offset columns ($D = 12$m, $KC \approx 1.7$) gives $C_D = 0.0$, halving the drag damping on these dominant members. In irregular waves, the broadband wave spectrum continuously feeds energy into the surge natural frequency, and the reduced damping permits catastrophic resonant build-up. The full-correction surge of 396.0 mm model-scale (19.8m full scale) is physically unrealistic and demonstrates that unconditional correction is inappropriate: the Steadiness correlations are not validated at such low KC values.

The adaptive correction restricts corrections to the crossbracing members ($D = 1.6$m, $KC \approx 8$–15), where $|\Delta C_D| > 0$ and the correction is physically justified. Nevertheless, the ensemble results show that the adaptive correction produces substantial response amplification (59%) in surge because the quadratic drag correction, proportional to $u_r|u_r|$, generates difference-frequency force components that span the low-frequency band including the surge natural frequency ($\omega_n \approx 0.40$ rad/s at model scale). With the extremely low surge damping ratio $\zeta_s \approx 0.0007$ (quality factor $Q \approx 700$), even small difference-frequency contributions from the brace corrections are amplified at resonance. This mechanism is analogous to the well-known slow-drift excitation of moored floating structures (Pinkster, 1980).

A frozen-switching diagnostic was conducted to quantify the feedback contribution of state-dependent switching for all 10 ensemble seeds. Switching decisions were computed from the uncorrected-state trajectory (which receives no corrections) and applied to the adaptive simulation without modification—decoupling the switching decision from the corrected state. The frozen-switching surge amplification of 259% (ratio of ensemble means) is statistically indistinguishable from the live-switching amplification of 259% (paired t-test

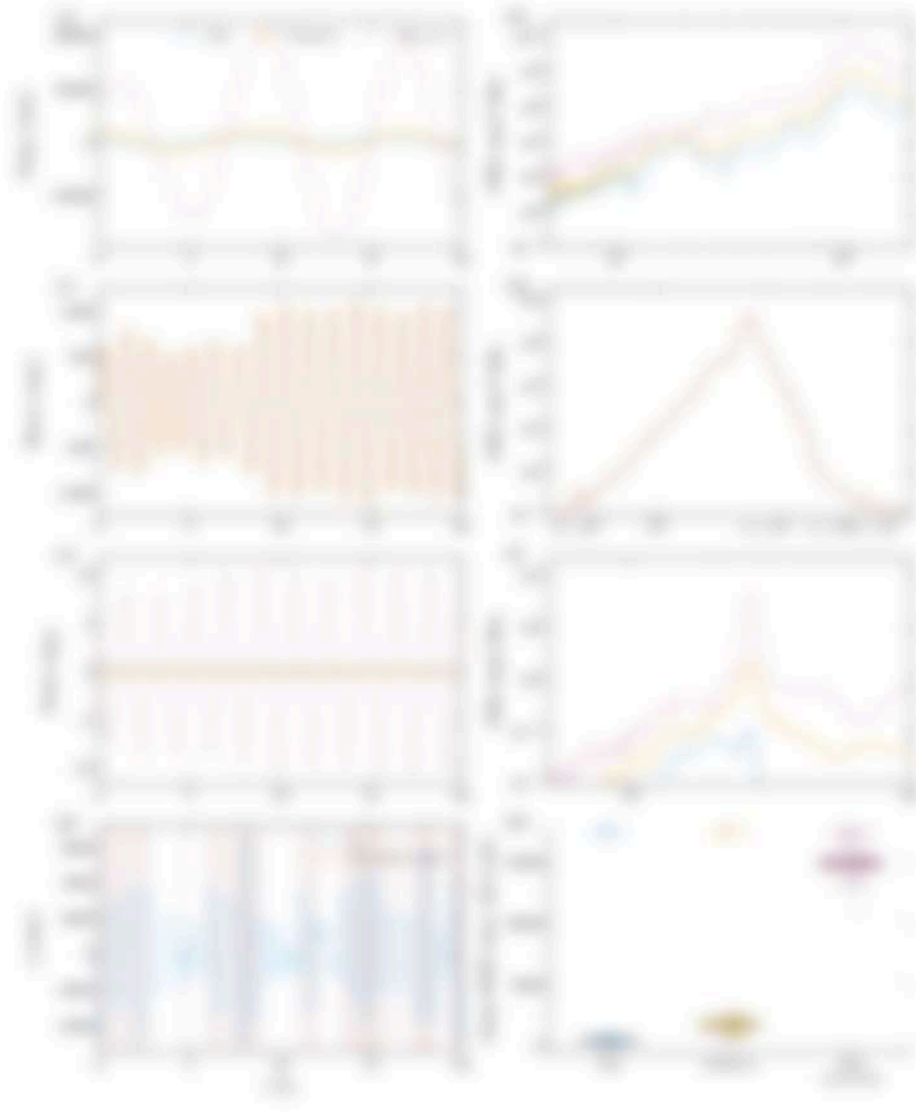

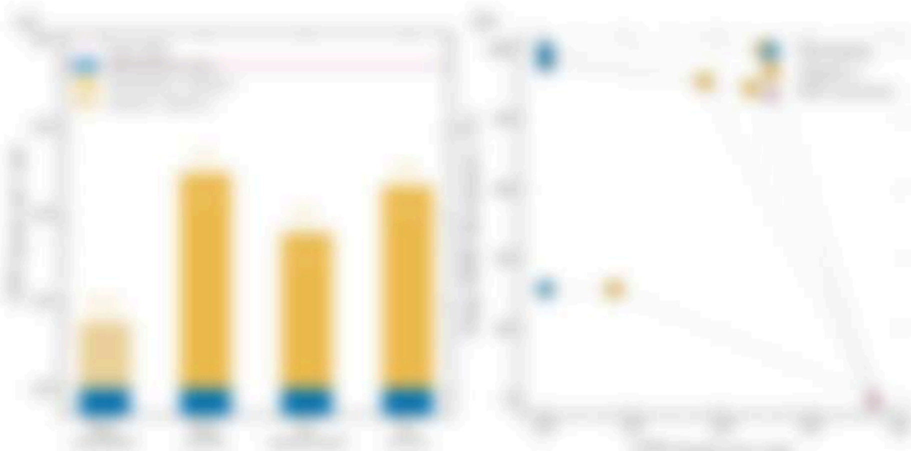

directed surge response through nonlinear energy transfer—an unexpected finding that underscores the importance of regime-appropriate coefficient selection for FOWT design. The full correction mode produces catastrophic resonant instability (30× surge amplification) when corrections are applied unconditionally to all members, as the Sarpkaya correlations below the drag damping on the offset columns at low KC.

Several limitations should be noted. First, the present study compares three variants of the same Cummins-equation solver and does not include validation against OC5 experimental wave response data; the comparisons demonstrate internal consistency and the diagnostic capability of the framework, but experimental validation is required before the framework can be used for design certification. Second, the wave excitation force uses a frequency-independent Froude–Krylov approximation with a constant diffraction correction factor; frequency-dependent excitation from a potential-flow solver (e.g., WAMIT or NEMOH) would improve the fidelity of the baseline model. Third, the Sarpkaya correlations below KC ≈ 3 are based on sparse experimental data with scatter exceeding ±30%; the catastrophic instability of the full-correction mode at low KC may partly reflect extrapolation uncertainty rather than true physics. Fourth, the numerical surge damping ratio ($\zeta_1 = 0.0007$) is 15–40× lower than values from physical model tests (Coulling et al., 2013); however, a parametric sweep from $\zeta_1 = 0.0007$ to 0.05 shows that the amplification ratio remains in the range 253–370%, indicating that the surge amplification is not an artifact of unrealistic damping. The absolute response levels, however, may differ for platforms with higher viscous damping or different mooring configurations.

The framework provides a systematic, physics-based approach for identifying modelling deficiencies in FOWT hydrodynamic analysis. Future work should validate the Sarpkaya-based reference model against 2D and 3D CFD simulations of oscillatory cylinder flow, extend the failure map to include diffraction effects on large-diameter members (which are not captured by the Morison equation), incorporate experimental or CFD-derived corrections for the column-scale hydrodynamics, and validate against the OC5 experimental measurements at

[illegible]

CRediT authorship contribution statement

[illegible]: Conceptualization, Methodology, Software, Validation, Formal analysis, Investigation, Data curation, Writing – original draft, Visualization. **[illegible]:** Supervision, Writing – review & editing, Funding acquisition.

Declaration of competing interest

The authors declare that they have no known competing financial interests or personal relationships that could have appeared to influence the work reported in this paper.

Data availability

All simulation input files and post-processing scripts will be made available on a public repository upon acceptance of the manuscript.

Acknowledgements

The authors acknowledge the use of the University of Oxford Advanced Research Computing facility.

References

[illegible], T., Windt, C., Davidson, J., Ringwood, J.V., 2022. A domain decomposition multi-fidelity approach for wave–body interaction problems. Applied Ocean Research 124, 103208. doi:10.1016/j.apor.2022.103208.

Coulling, A.J., Goupee, A.J., Robertson, A.N., Jonkman, J.M., Dagher, H.J., 2013. Validation of a FAST semi-submersible floating wind turbine numerical model with DeepCwind test data. Journal of Renewable and Sustainable Energy 5, 023116. doi:10.1063/1.4796197.

global loads of the DeepCwind floating semisubmersible wind turbine. Energy Procedia 137, 38–57. doi:10.1016/j.egypro.2017.10.333.

Sarpkaya, T., 1976. Vortex shedding and resistance in harmonic flow about smooth and rough circular cylinders at high Reynolds numbers. Technical Report NPS-59SL76021. Naval Postgraduate School.

Sarpkaya, T., 1986. Force on a circular cylinder in viscous oscillatory flow at low Keulegan–Carpenter numbers. Journal of Fluid Mechanics 165, 61–71. doi:10.1017/S0022112086003014.

Stansby, P.K., Moreno, E.C., Stallard, T., 2017. Large capacity multi-float configurations for the wave energy converter M4 using a time-domain linear diffraction model. Applied Ocean Research 68, 53–64. doi:10.1016/j.apor.2017.06.007.

Sumer, B.M., Fredsøe, J., 2006. Hydrodynamics Around Cylindrical Structures. Revised ed., World Scientific.

Tran, T.T., Kim, D.H., 2015. The coupled dynamic response computation for a semi-submersible platform of floating offshore wind turbine. Journal of Wind Engineering and Industrial Aerodynamics 147, 104–119. doi:10.1016/j.jweia.2015.09.016.

Wang, L., Robertson, A., Jonkman, J., Yu, Y.H., 2021. OC6 phase Ib: Validation of the CFD predictions of difference-frequency wave excitation on a FOWT semisubmersible. Ocean Engineering 241, 110026. doi:10.1016/j.oceaneng.2021.110026.